Materials Advances

ROYAL SOCIETY OF CHEMISTRY

PAPER

View Article Online
View Journal

Cite this: DOI: 10.1039/d6ma00417b

Hierarchically structured mixed-linker HKUST-1 metal–organic frameworks as catalysts: one-pot synthesis of quinazolines

Anna Nowacka and Francesc X. Llabrés i Xamena *

Received 26th March 2026,
Accepted 30th April 2026

DOI: 10.1039/d6ma00417b

rsc.li/materials-advances

Hierarchically structured HKUST-1 compounds have been prepared *via* a mixed-linker strategy starting from mixtures of trimesic (BTC) and 5-hydroxyisophthalic (OH-IP) acids in different proportions. Unlike purely microporous pristine HKUST-1, the mixed-linker compounds feature a hierarchical micro-/mesoporous system in which mesopores account for up to 40% of the total pore volume of the solid. The creation of mesopores is reflected by the appearance of deep trenches running in well-defined directions, parallel to the edges of the octahedral crystal. This demonstrates that point defects introduced by the incorporation of OH-IP are not distributed randomly throughout the framework, but they tend to coalesce into line defects along the ⟨110⟩ direction. The creation of such a hierarchical system of mesopores translates into a higher catalytic activity of mixed-linker MOFs with respect to pristine HKUST-1 for the conversion of bulky substrates, as we showed for the synthesis of quinazoline by oxidative coupling of benzylamine and 2-aminoacetophenone with *tert*-butyl hydroperoxide.

1. Introduction

For over two decades, metal–organic frameworks (MOFs) have been recognized for their significant utility as heterogeneous catalysts.[1–3] Their remarkable properties, including exceptionally large surface areas, a high degree of tunability in their pore structure and chemical composition, and the inherent capacity for post-synthesis modification, collectively position MOFs as highly promising candidates for the development of advanced heterogeneous catalysts. These attributes enable the design of catalysts exhibiting superior activity and specificity, thereby addressing the demands of a broad spectrum of applications. However, a substantial quantity of MOFs exhibit microporosity (pore diameter < 2 nm), which can significantly restrict their utility in applications involving bulky substrates.[4] This limitation arises from diffusion constraints and restricted access to the active metal sites within the MOFs.[5] Therefore, considerable efforts have been directed towards expanding the pore dimensions of MOFs into the mesoporous range.[6,7]

One way of achieving this goal involves the controlled generation of large-scale defects within the crystalline framework in a controlled way, leading to the formation of hierarchically structured MOFs. A number of *de novo* methodologies have been reported to date, including ligand extension or hydrolytic post-synthesis methods, among others.[8]

One specific technique that has attracted considerable attention is metal–ligand–fragment co-assembly,[9] also known as the defective linker approach.[10–13] The method comprises combining the native organic linker of the parent MOFs with a small amount of a truncated defect-inducing linker, which is geometrically equivalent but lacks one or more connecting functional groups. The large-scale arrangement of such defects (*e.g.*, point-defect clustering) can lead to the formation of mesopores within the crystal structure. The resulting defective materials are called hierarchically structured MOFs, in which micro- and mesopores coexist without compromising the crystalline integrity of the material. The presence of mesopores can greatly influence mass transport pathways within the pore system, as well as the framework's rigidity and density, its electronic and magnetic properties, and ultimately the material's catalytic performance.[14–16]

In relevant prior reports, Fang *et al.*[17] reported on the synthesis of a series of defect-engineered MOFs based on HKUST-1 by mixing the native trimesate struts with various defect-inducing linkers (*viz.*, 5-hydroxyisophthalate and pyridine-3,5-dicarboxylate linkers) in varying ratios, as a way to control the properties of the metal nodes and to introduce functionalized mesopores simultaneously. Analogously, Liu *et al.*[18] partially replaced trimesate linkers in HKUST-1 with benzoic acid as a defect-inducing linker, resulting in hierarchical micro–mesoporous systems with improved external surface area compared to the pristine MOF. Besides HKUST-1, we also reported the use of a mixed-linker synthesis approach to modulate the textural and catalytic properties of zirconium trimesate MOF-808 as heterogeneous

Instituto de Tecnología Química (ITQ), Consejo Superior de Investigaciones Científicas-Universitat Politècnica de València, 46022, Valencia, Spain. E-mail: fllabres@itq.upv.es, anna.nowacka21@gmail.com

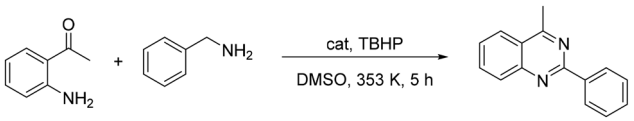

Scheme 1 Typical reaction conditions for the cyclization of 2-aminoacetophenone and benzylamine.

catalysts for the Meerwein–Ponndorf–Verley reduction of bulky carbonyl compounds, such as ketosteroids.[4,19]

Herein, we describe the use of a defective-linker approach to prepare copper trimesate HKUST-1 compounds exhibiting hierarchical micro–mesoporosity. We analyze the impact of the induced defects and hierarchical pore structure on the catalytic performance of the modified compounds in a reaction involving sterically hindered products, in comparison with unmodified HKUST-1. For this investigation, we have considered the one-pot oxidative synthesis of quinazoline (with approximate dimensions of 12 × 8 × 3 Å^3) as a model reaction (see Scheme 1), given its molecular dimensions are comparable to the pore openings of HKUST-1 (approximately 9 Å in diameter).

N-Heterocycles are present in many natural products and are well known biological active molecules, and quinazoline and quinazolinone skeletons are recurrently found in the pharmaceutical literature.[20] Quinazolines are conventionally prepared *via* Bischler cyclization of dicarbonyl compounds and diamines, but novel synthetic pathways are actively being investigated.[21] Thus, Wang *et al.*[22] reported on a simple and efficient, ligand-free Cu^+ catalyzed Ullman coupling and aerobic oxidation route to quinazoline derivatives, by reacting substituted (2-bromophenyl)methylamines with amides. In another report by Han *et al.*,[23] CuCl/DABCO/4-HO-TEMPO was used as a catalyst for the aerobic oxidative synthesis of 2-substituted quinazolines through a one-pot reaction between aldehydes and 2-aminobenzylamines. Despite the good results obtained with homogeneous catalysts, developing heterogeneous catalysts for the synthesis of quinazoline remains a consistently practical and compelling alternative. In this sense, γ-Fe_2O_3 nanoparticles[24] and polymer-supported bimetallic Pt/Ir alloyed nanoclusters[25] have been reported for this reaction. Also, MOFs have been considered for this reaction. Truong *et al.*[26] reported on the use of cobalt-containing ZIF-67 for the cyclization of 2-aminobenzoketones and benzylamines, yielding 2-arylquinazolines, with results indicating high activity and reusability.

2. Experimental

2.1. Synthesis

We have used the mixed-linker solid solution method to prepare two hierarchically structured copper-containing HKUST-1 compounds, referred to as **HM-1** and **HM-2**. A pristine, linker pure HKUST-1 material, named **M-1**, was also prepared for comparison. We followed a slightly modified method reported earlier,[17] using mixtures of trimesic acid (H_3BTC) and 5-hydroxyisophthalic acid (OH-IP) in different proportions. For the synthesis of the pristine **M-1** compound, $Cu(NO_3)_2{\cdot}2.5H_2O$ (5 mmol) was dissolved in 25 mL of H_2O. Then, a second solution of H_3BTC (2.5 mmol) in 25 mL of DMF was prepared, and both solutions were mixed under stirring, transferred into an autoclave and placed inside an oven at 373 K for 4 h. The blue precipitate obtained was filtered off, thoroughly washed with DMF and soaked three times for 6 hours with methanol and dried under a vacuum at 573 K overnight before use.

Mixed-linker **HM-1** and **HM-2** compounds were prepared and purified using an analogous procedure and starting from a mixture of linkers with different BTC : OH-IP ratios of 70 : 30 and 50 : 50, respectively.

2.2. Characterization

Powder X-ray diffraction (PXRD) was used to confirm the expected structure and crystallinity of the materials. Powder material analysis was performed on a PANalytical Cubix fast diffractometer, using CuKα1 radiation (λ = 1.5406 Å) and an X'Celerator detector with Bragg–Brentano geometry. XRD patterns recorded in the 2θ range from 2 to 60 were analyzed using X'pert Highscore Plus software. The corresponding thermogravimetric (TGA) curves of the MOFs were obtained in the temperature range of 300–700 K under an air flow and a heating ramp of 10 K min^{-1} using a Netzsch STA 449 F3 Jupiter analyzer. The BTC:OH-IP ratios of samples **HM-1** and **HM-2** were determined by Nuclear Magnetic Resonance (NMR) on a Bruker Avance spectrometer of 300 MHz frequency using TMS as an internal standard and normalizing the signals to the DMSO-d_6 signal. To do this, liquid phase ^{1}H NMR spectra were recorded for the samples (30 mg) digested in d_2-H_2SO_4 (0.1 mL) and d_6-DMSO (0.5 mL) mixtures. N_2 adsorption–desorption isotherms at 77 K were collected on a Micrometrics Gemini V gas adsorption analyzer. The specific surface area (S_{BET}) was obtained using the BET method (in the P/P_0 0.01 to 0.1 range) after fulfilling the four consistency criteria recommended by Rouquerol.[27,28] Pore size distribution was determined from the BJH method applied to the adsorption branch.[29] Specific external surface area (S_{ext}) and micropore volume (V_{micro}) were determined from the corresponding *t*-plot analysis. Morphology of the samples was analyzed by field emission scanning electron microscopy (FESEM) using a Zeiss Ultra55 instrument. In the leaching experiment, metal traces in the reaction filtrate were analyzed by ICP-OES on a Varian 715-ES instrument.

2.3. Catalytic reaction

In a typical catalytic test, 20 mg of the as prepared catalyst was added to a glass reactor containing a mixture of 2-aminoacetophenone (122 μL, 1 mmol), benzylamine (164 μL, 1.5 mmol), *tert*-butyl hydroperoxide (TBHP) 70% in water (685 μL, 5 mmol), and diphenyl ether (100 μL) as an internal standard in DMSO (2 mL). The reaction mixture was stirred for 5 h at 400 rpm (enough to avoid external diffusion control of the reaction), at 353 K. The reaction conversion was monitored by withdrawing aliquots from the reaction mixture at different time intervals, quenched with an aqueous KOH solution (5%, 1 mL), dried over anhydrous Na_2SO_4, and analyzed by GC with reference to diphenyl ether. An Agilent 7890A instrument equipped with a

flame ionization detector (FID) and a HP5 column (30 m × 0.25 mm × 0.25 μm) was used.

3. Results and discussion

3.1. Synthesis and characterization

Pristine HKUST-1 (**M-1**) and mixed-linker **HM-1** and **HM-2** samples were obtained as described in the Experimental section. The corresponding PXRD patterns shown in Fig. 1 are in perfect agreement with the pattern simulated for HKUST-1, indicating that all materials are isoreticular, pure compounds with high crystallinity. The XRD patterns of **HM-1** and **HM-2** show no evidence of peak splitting or any significant peak broadening, thus ruling out the formation of a mixture of two phases. Moreover, an eventual phase pure OH-IP copper MOF would necessarily have a different crystalline structure, leading to the appearance of additional peak lines not attributable to the HKUST-1 material, which are not observed in any case.

The amounts of OH-IP incorporated into **HM-1** and **HM-2** were determined from the peak intensity ratio in the corresponding ^{1}H NMR spectra after digestion of the samples in d_2-H_2SO_4/d_6-DMSO mixtures (Fig. S1 in the SI). The analysis revealed that **HM-1** and **HM-2** contained 10% and 15% of the OH-IP linker, respectively.

The thermal stability of the pristine and mixed-linker samples was determined from the TGA curves (Fig. S2). All three samples showed the typical two-step weight loss expected for HKUST-1 compounds: a first weight loss of *ca.* 30 wt% at around 350 K, due to coordinated water, and a second weight loss of *ca.* 45 wt% between 550 and 600 K due to linker decomposition. The compared TGA curves indicate that the thermal stability of mixed-linker samples with respect to pristine HKUST-1 gradually decreases with the amount of OH-IP incorporated in the structure, as it can be better appreciated in the derivative curves (Fig. S2). Thus, linker decomposition starts at 583 K in pure **M-1**, while for **HM-1** and **HM-2**, the process starts at 563 K and 553 K, respectively.

Following the method reported by Valenzano *et al.*,[30] the TGA curves were also used to estimate the relative metal-to-linker content of the materials, which allows us to determine whether ligand or metal defects (which are not mutually exclusive) predominate within a material, and in what proportion. Combining this information with the data coming from ICP (Cu) and elemental analysis (C, H, N), the chemical composition and empirical formulas of the samples were determined, and the results are summarized in Table 1 (and related information in the SI).

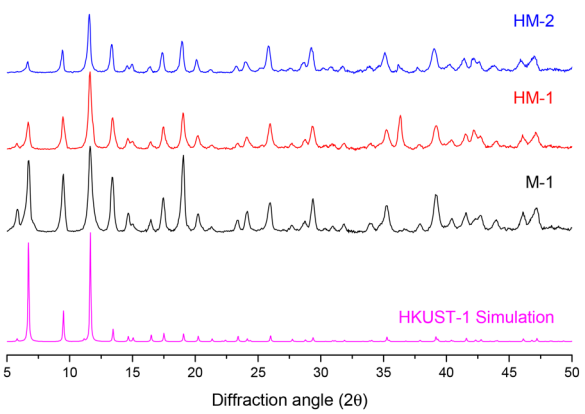

Fig. 1 XRD patterns (CuKα1 radiation) of pristine HKUST-1 (**M-1**) and hierarchically structured samples **HM-1** and **HM-2**.

Table 1 Empirical formulas and missing linker defects determined for the samples

	Empirical formula	Missing linkers (%)
M-1	$[Cu_3(BTC)_{1.94}]$	3.0
HM-1	$[Cu_3(BTC)_{1.73}(OH\text{-}IP)_{0.19}(NO_3)_{0.19}]$	4.0
HM-2	$[Cu_3(BTC)_{1.54}(OH\text{-}IP)_{0.27}(NO_3)_{0.27}]$	9.5

The empirical formula of "ideal", defect-free HKUST-1 is $[Cu_3(BTC)_2]$. However, it is well known that "real" MOFs usually contain structural defects, such as missing linkers, missing metallic nodes, or both types of defects simultaneously. These missing units all contribute to enhancing the porosity of the defective material (*vide infra*). According to our TGA, the total amount of organic linkers (BTC + OH-IP) in all the samples prepared is lower than 2, the value expected from the theoretical formula for "ideal" HKUST-1, indicating that in all of them there is a neat predominance of missing linker defects over missing metallic nodes. The calculated net amount of missing linker defects is quite low in **M1** and **HM-1** (3–4%), and it increases significantly in **HM-2** (up to 9.5%).

Moreover, when mixed-linker MOFs are prepared by combining BTC^{-3} linkers with ditopic $OH\text{-}IP^{-2}$, as in **HM-1** and **HM-2** samples, the excess charge of the missing carboxylate of OH-IP with respect to trivalent BTC^{-3} linkers can be compensated by: (i) residual anions (NO_3^-) coming from the copper nitrate used in the synthesis, (ii) mixed-valence Cu^+/Cu^{2+} species, or (iii) missing Cu_2 paddlewheel nodes. Since TGA has shown that there are fewer metallic node defects than linker defects, and FTIR spectroscopy of adsorbed CO revealed that the amounts of Cu^+ centers in all samples are similar and very low (see discussion below), it is assumed that charge defects upon OH-IP incorporation are mainly compensated by residual nitrate anions, as it has been reflected in the calculated empirical formulas shown in Table 1.

The textural properties of the samples were then evaluated from the N_2 adsorption–desorption isotherms at 77 K, and the curves obtained are shown in Fig. 2. The pristine **M-1** sample exhibits a clear type-I isotherm,[31] with a sharp increase in the N_2 uptake at a low relative pressure, followed by a plateau, typical of microporous HKUST-1.[32] A small hysteresis loop, akin to H3 o H4 type according to the IUPAC classification,[33] is observed at high relative pressures, indicating the presence of interparticle porosity.

Conversely, **HM-1** and **HM-2** show distinctly different, type IV isotherms, with well-defined H2 type hysteresis loops at relative pressures of $P/P_0 > 0.4$, indicating capillary condensation of N_2 in mesopores. Thus, these results prove the coexistence of a

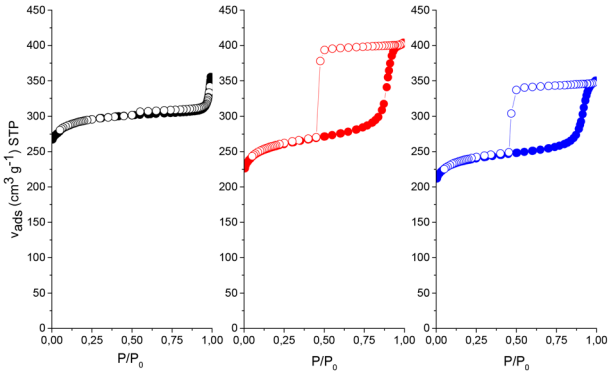

Fig. 2 N_2 adsorption–desorption isotherms (at 77 K) of (from left to right) **M-1**, **HM-1** and **HM-2** samples.

Table 2 Textural properties of the samples

	S_{BET} ($m^2\ g^{-1}$)[a]	Pore volume ($cm^3\ g^{-1}$)			Pore diameter (nm)
		V_{tot}[b]	V_{micro}[c]	V_{meso}[d]	
M-1	1166	0.550	0.449	0.036	No mesopores
HM-1	1008	0.625	0.371	0.240	1.98
HM-2	939	0.542	0.351	0.149	2.48

[a] S_{BET}: Brunauer–Emmett–Teller surface area. Only data points satisfying the Rouquerol consistency criterion have been considered. [b] V_{total}: total pore volume, calculated from the nitrogen adsorption data at P/P_0 = 0.995. [c] V_{micro}: micropore volume obtained using the *t*-plot method. [d] V_{meso}: mesopore volume calculated using the Barrett–Joyner–Halenda (BJH) method.

hierarchical system of micro- and mesopores in mixed-linker **HM-1** and **HM-2** samples.

Table 2 shows a summary of the textural properties for the samples, calculated as detailed in the Experimental section.

According to the data presented in Table 2, incorporation of the OH-IP linker into the crystalline framework of HKUST-1 produces a gradual decrease of the S_{BET} value with respect to the pristine sample. This can be attributed to an increase in the pore size in hierarchical MOFs,[9] which in the case of **HM-1** and **HM-2** is 1.98 and 2.48 nm, respectively. S_{BET} values can also be affected by a decrease in the crystallinity of **HM-1** and **HM-2** samples due to the formation of structural defects induced by the introduction of the secondary linker in the structure.[18] Indeed, the presence of mesopores accompanied by a certain loss of specific surface area has been previously observed in many works related to the preparation of mixed-linker MOFs and other compounds.[9,18,22–26,34] While **M-1** is basically microporous (V_{meso} = 0.036 $cm^3\ g^{-1}$), **HM-1** and **HM-2** samples exhibit a significant mesopore volume, accounting for up to 40% of the total pore volume in **HM-1** and a slightly lower 30% in **HM-2**.

In comparison with other pristine and mixed-linker HKUST-1 samples prepared with the OH-IP ligand as reported by other researchers,[17] our synthesized materials exhibit notably lower specific surface areas and total pore volume values. For instance, 1882 $m^2\ g^{-1}$ and 0.773 $cm^3\ g^{-1}$, contrasting with 1166 $m^2\ g^{-1}$ and 0.550 $cm^3\ g^{-1}$ for pristine HKUST-1, and S_{BET} values of approximately 1700–1800 $m^2\ g^{-1}$ and pore volumes of about 0.75 $cm^3\ g^{-1}$, compared to surface areas of around 1000 $m^2\ g^{-1}$ and pore volumes of 0.54–0.62 $cm^3\ g^{-1}$. These disparities are significant and are likely attributable to reduced crystallinity and the potential incorporation of amorphous material within our samples, relative to those synthesized by Fang *et al.*[17]

Formation of mesopores in mixed-linker HKUST-1 has been previously reported by Fang *et al.*[17] Incorporation of OH-IP linkers into the crystalline framework introduced a charge excess due to the different charge of $[BTC]^{3-}$ and $[OH\text{-}IP]^{2-}$ linkers. The authors proposed that charge excess can be compensated either by the partial reduction of Cu^{2+} to Cu^{+} in the inorganic building blocks or by the presence of missing linker defects or missing copper nodes. Both mechanisms would result in the formation of local defects, which subsequently facilitate the creation of mesopores through their clustering. Nevertheless, the authors did not determine in their original work whether the introduction of OH-IP defective linkers and creation of mesopores in mixed-linkers HKUST-1 induced any alterations in particle morphology.

Fig. 3 and Fig. S3 show FESEM images of **M-1**, **HM-1** and **HM-2** samples. As can be seen, **M-1** exhibits well-formed octahedral crystallites typical of HKUST-1 materials, with sharp edges and some inherent defects on their faces, formed during the crystallization process.[35] The same morphology is also observed for mixed-linker **HM-1** and **HM-2** samples, though surface defects become gradually more evident and ordered upon OH-IP incorporation, while the edges of the octahedra become more rounded.

Other authors have also reported important morphology changes in HKUST-1 prepared in the presence of benzoic acid or citric acid modulators.[18,36] In those cases, the authors described the formation of relatively big holes randomly distributed on the surface of the octahedral crystals. Interestingly, the type of defects created in **HM-1** and **HM-2** upon incorporation of OH-IP linkers is clearly not randomly distributed on the crystallite faces, in evident contrast with the meso/macropores created during the synthesis with benzoic or citric acid modulators. Instead, these defects tend to coalesce into extensive linear trenches that run parallel to the edges of the octahedral crystals. The observed trenches in **HM-1** and **HM-2** exhibit a resemblance to defect lines also oriented parallel to the octahedral edges, as reported by Shöâeè *et al.*[35,37] and by Ameloot *et al.*,[38] using atomic force microscopy (AFM) and *operando* confocal fluorescence microscopy, respectively. The authors attributed the formation of these defect lines to dislocations of the crystalline network along the ⟨110⟩ direction. Projection of the HKUST-1 structure along the ⟨110⟩ direction indicates two potential surface terminations for the {111} planes (corresponding to triangular faces of the octahedra) that do not involve the cleavage of intramolecular bonds within the BTC linkers. Of these two viable surface terminations, the one depicted in Fig. 4 is considered the most feasible, wherein only a single carboxylate group per BTC linker remains unbound to the bulk crystal structure.

It is logical to postulate that OH-IP linkers, possessing only two carboxylate groups as opposed to the three found in BTC, may preferentially occupy these sites at the {111} surface terminations.

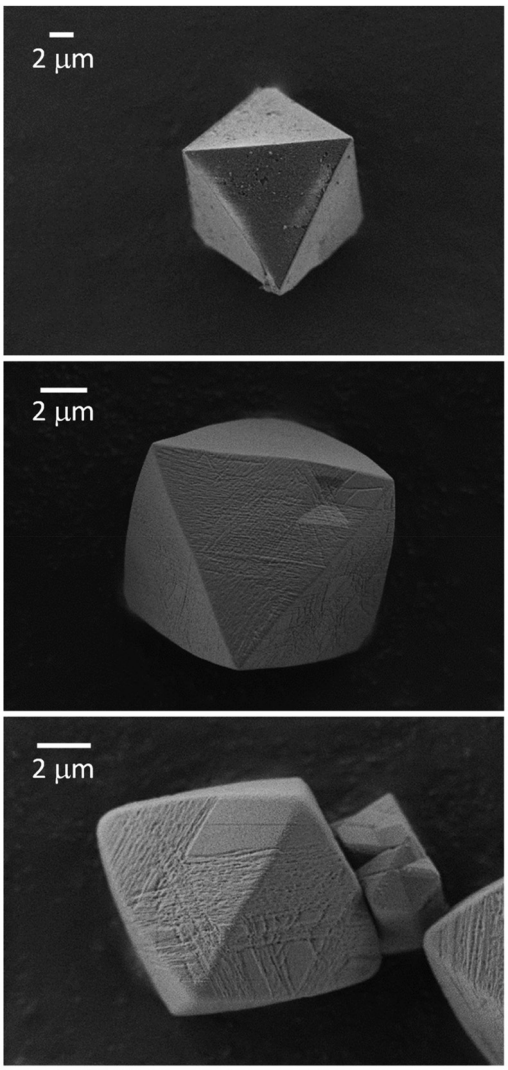

Fig. 3 FESEM images of (from top to bottom) **M-1**, **HM-1** and **HM-2**.

Consequently, the hydroxyl group of OH-IP (represented by a large green sphere in the figure) would extend outwards from the triangular faces of the octahedral crystals, while the linker would maintain its connection to the crystal *via* the two remaining carboxylate groups. Therefore, as the amount of OH-IP incorporated within the solid network increases (passing from **HM-1** to **HM-2**), a higher concentration of defective linkers at these surface termination sites is anticipated. This observation may account for the formation of extended line defects that run parallel to the edges of the octahedral crystals. In other words, the analysis of the surface morphology of our mixed-linker samples has revealed that the distribution of OH-IP linkers within the HKUST-1 crystal lattice would not be random but rather ordered along defect lines, thereby leading to the formation of broad and deep trenches evidenced in the aforementioned FESEM images.

We have carefully evaluated the relative peak intensities and the peak width of all the diffraction lines in all three samples, but we have not found any clear correlation with the amount of OH-IP linker incorporation. This might be related to the relatively low

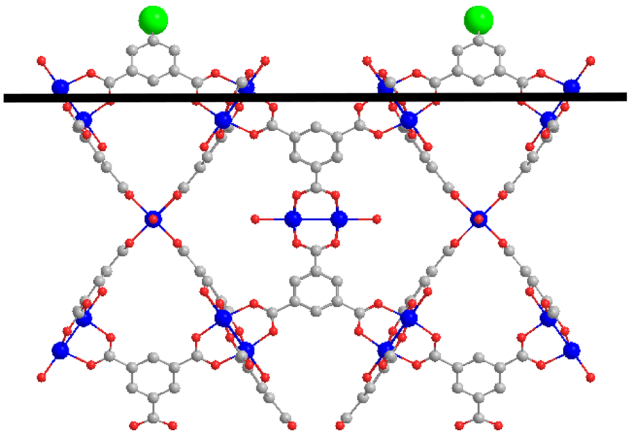

Fig. 4 Structure of HKUST-1 viewed along the ⟨110⟩ direction, showing the most likely surface termination at the {111} faces. The green spheres represent the dangling hydroxy groups of OH-IP linkers pointing outwards from the triangular faces of the octahedral crystals, while the broad black line represents the terminations of these triangular {111} faces.

substitution of OH-IP linkers in samples **HM-1** and **HM-2**, but it is likely not the only factor. Note that incorporation of the OH-IP linker in the HKUST-1 lattice can disrupt the crystal growth of the MOF in the direction where the OH groups are oriented, giving rise to the formation of the wide trenches observed in the FESEM images, but without affecting the crystallographic planes underneath these terminations. A much more detailed diffraction analysis, probably combined with other advanced techniques more sensitive to surface atoms (such as SEXAFS) and quantum chemical calculations, would be required to determine this point, which falls beyond the scope of the present paper.

3.2. Synthesis of quinazoline

As mentioned before, we selected the formation of a bulky compound as a test reaction to evaluate the benefits of a hierarchical micro-/mesopore system in mixed-linker HKUST-1. Thus, herein we have carried out the oxidative synthesis of quinazoline from 2-aminoacetophenone and benzylamine in the presence of **M-1**, **HM-1** and **HM-2** catalysts, using TBHP as the oxidant in DMSO at 353 K (Scheme 1). The results obtained up to 5 h of reaction time are shown in Fig. 5. A blank experiment (without using any catalyst) was also performed under the same reaction conditions, but no quinazoline yield was obtained even after extending the reaction for 8 h.

All three compounds showed good activity and quantitative selectivity to quinazoline, and no other products were detected. However, a definite increase in the reaction rate and final conversion was observed upon increasing the amount of OH-IP incorporated into the MOF structure. Thus, the yield obtained after 3 h of reaction was 54%, 68% and 91% for **M-1**, **HM-1** and **HM-2** catalysts, respectively. While **M-1** showed a clear induction period of approximately 1 h prior to quinazoline formation, this lag phase was progressively suppressed for the hierarchically structured MOFs. The sample **HM-2**, containing 15% of OH-IP incorporated into the framework, demonstrated the best catalytic performance, achieving a quinazoline yield of

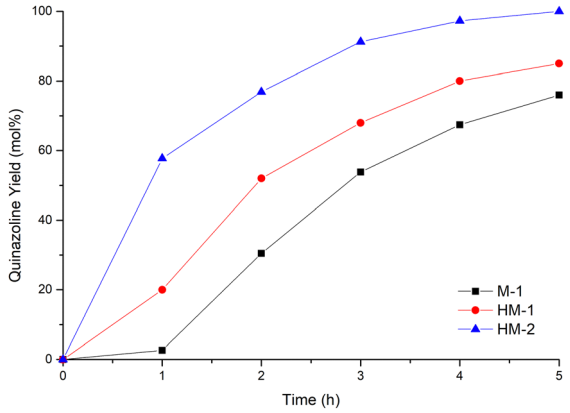

Fig. 5 Time–yield plot of oxidative quinazoline synthesis over **M-1**, **HM-1** and **HM-2** catalysts.

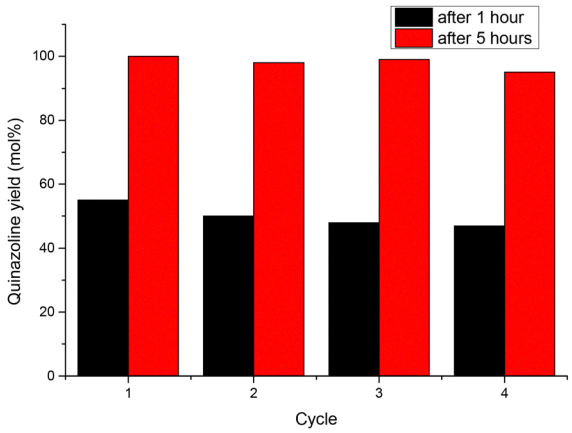

Fig. 6 Reusability of **HM-2** after 1 h and 5 h of reaction time.

100% within 5 hours. Therefore, this catalyst was selected for further evaluation.

The scope of the reaction was evaluated by applying the process to the synthesis of other quinazolines, including bulkier substrates, such as 2-aminobenzophenone, as well as substituted benzylamines with electron donating or electron withdrawing groups in the *para* position (Table S1). In all cases, the reaction was 100% selective to the corresponding quinazoline derivatives, while the presence of mesoporosity in **HM-2** ensured excellent yields for all the compounds tested.

To demonstrate the heterogeneous character of the reaction and to exclude the possibility of active species leaching from the solid phase into the liquid reaction medium, a hot filtration experiment was carried out during the course of the reaction. Thus, the quinazoline synthesis reaction was carried out under the same reaction conditions for 0.5 h in the presence of **HM-2**. At this point, with a 24% quinazoline yield, the solid catalyst was separated from the reaction mixture by filtration at the reaction temperature, and the reaction was continued for an additional 4.5 h in the absence of the catalyst. The results obtained (Fig. S4) showed that the reaction almost completely stopped after the catalyst was removed, with practically no further quinazoline formation observed. Furthermore, the ICP analysis of the filtrate after the reaction indicates that no significant leaching of the active copper species took place. These results clearly show that the cyclization reaction between 2-aminoacetophenone and benzylamine only proceeds in the presence of the catalyst and that the process is truly heterogeneous.

Finally, we evaluated the reusability of the catalyst. Thus, **HM-2** was reused in consecutive catalytic cycles under identical reaction conditions. After each run for 5 h, the solid was recovered by centrifugation, washed with fresh DMSO and acetone, dried overnight at room temperature under a vacuum and reused in consecutive cycles.

As shown in Fig. 6, **HM-2** showed an excellent reusability for at least four cycles, with only a minor loss of activity and keeping the full selectivity to quinazoline. Thus, the quinazoline yield after 1 h gradually decreases from 55% in the first cycle to 47% in the fourth cycle, while the full conversion after 5 h is maintained in all runs. The XRD pattern of the solid recovered after four catalytic runs (Fig. S5) showed a small decrease in the intensity of the diffraction peaks with respect to the fresh material, which is probably due to the adsorption of reaction products on the surface of the catalysts that are not completely removed during the washing procedure, though some actual crystallinity loss can also take place due to the mechanical attrition of the particles during the reaction. Nevertheless, the overall structural integrity of the catalyst is clearly preserved throughout all the uses.

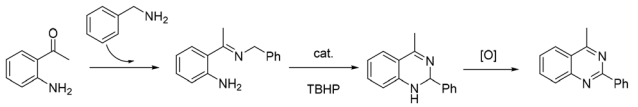

Scheme 2 Mechanism of the oxidative coupling synthesis of quinazoline.

Based on previous related studies, a plausible mechanism to explain the one-pot formation of quinazoline through oxidative coupling of benylamine and 2-aminoacetophenone is depicted in Scheme 2.

First, an intermediate imine product is formed by the condensation of 2-aminoacetophenone and benzylamine. This step is almost immediate and it can take place under catalyst free conditions. However, the coordinatively unsaturated Cu^{2+} sites in HKUST-1 can act as Lewis acid sites to accelerate this step even further. Then, the imine intermediate undergoes an oxidative cyclization reaction in the presence of TBHP, which finally yields the target quinazoline product by oxidative dehydrogenation.

3.3. Origin of the higher catalytic activity of hierarchically structured MOFs

Several authors have reported on the use of defective linkers to improve the catalytic performance of MOFs as well as a means of introducing new properties that are totally absent in the unmodified, pristine material.[4,19,39] In most cases, the improvement of the catalytic properties of mixed-linker MOFs is attributed to the creation of point defects, leading to the creation of more exposed and/or more reactive active sites. In the particular case of compounds with the HKUST-1 structure, creation of mixed-

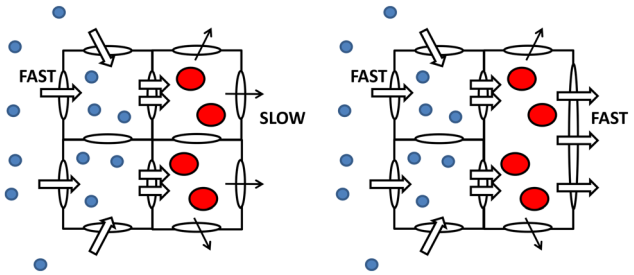

Fig. 7 Diffusion of small reactants (blue spheres) and bulky products (red spheres) in pristine microporous **M-1** (left) and hierarchical mesoporous–mesoporous materials **HM-1** and **HM-2** (right).

valence copper or ruthenium centers upon incorporation of defective linkers was deemed responsible for the higher reactivity in the oxidation of benzene derivatives,[40] olefin hydrogenation, CO_2 reduction[12] or Paal–Knorr synthesis of pyrrole.[13] Thus, a similar effect might also be behind the higher catalytic activity of mixed-linker compounds for the synthesis of quinazoline observed in the present work. In other words, partial substitution of BTC by OH-IP linkers can create defective sites similar to those observed in other mixed-linker MOFs. However, FTIR spectroscopy of adsorbed CO at 77 K onto **M-1** and **HM-2** (see Fig. S6) revealed that no significant differences exist in the type, amount or accessibility of the active sites in both materials. Thus, we did not observe any higher amount of reduced Cu^+ sites in **HM-2** than in **M-1** as a consequence of the introduction of OH-IP linkers into the framework, since this would be seen in appreciable changes in relative intensities of the corresponding IR absorption bands upon CO adsorption on these reduced sites. Thus, even if the creation of a small population of partially reduced sites cannot be totally excluded, the higher activity of **HM-2** for the quinazoline synthesis may have a different origin.

In our opinion, the catalytic results shown in Fig. 5 and Table S1 can be explained by the presence of a hierarchical micro-/mesopore system in **HM-1** and **HM-2**. While the reagents benzylamine and 2-aminoacetophenone used in this reaction are small enough to enter and freely diffuse inside the pores of HKUST-1 (with a diameter of *ca.* 9 Å), this is not so for the bulky quinazoline product, with approximate dimensions of $12 \times 8 \times 3$ Å^3, very close to the pore openings of the MOF. Thus, once quinazoline is formed inside the MOF pores (where the active sites are located), strong diffusion limitations are anticipated for its desorption,[5] increasing the time of residence of the reaction products inside the pores and partially blocking the access of fresh reactants to the active sites. However, the presence of a mesopore system in mixed-linker **HM-1** and **HM-2** (accounting for up to 40% of the total pore volume of the material) can provide an alternative diffusion pathway for a fast quinazoline desorption, thus minimizing the unwanted pore-blocking, which would translate into a higher reaction rate, as it is schematically depicted in Fig. 7.

Besides the aforementioned benefits of the creation of a hierarchical mesoporous system in mixed-linker MOFs, other factors might contribute as well to the observed catalytic properties of **M-1** *vs.* **HM-1**/**HM-2**. One of them could be particle size: smaller crystallites would reduce the diffusion path length, thereby minimizing mass transport limitations. However, according to the FESEM images shown in Fig. 3 (and additional images shown in Fig. S3), the average particle size is close to 10–12 μm for all compounds, with no significant differences among them. Moreover, the relatively large particle size of all three materials indicates that most active sites are located in the internal surface of the catalysts, so that the contribution from external sites to the overall catalytic activity is expected to be low.

4. Conclusion

Herein we describe the preparation of isoreticular mixed-linker HKUST-1 materials in which the parent BTC linker has been partially replaced by a defect-inducing ditopic linker, OH-IP. As a result, a hierarchical micro-/mesoporous system is formed, in which mesopores account for up to 40% of the total pore volume, accompanied by a slight decrease of the specific surface area (S_{BET}), from 1166 to 939 m^2 g^{-1}. A close inspection of the morphology of the crystals by means of FESEM showed that mesopores are well visible in the form of deep trenches that run parallel to the edges of the octahedral crystals. These trenches are compatible with dislocations along the ⟨110⟩ direction, which would lead to preferential surface terminations in the {111} faces in which the linkers are bound to the bulk crystals by only two carboxylate groups, while the third one is dangling. It is reasonable that these terminal positions are preferentially occupied by ditopic OH-IP linkers; as the amount of OH-IP incorporated into the framework increases, the number and depth of the trenches are also seen to increase.

Pristine and mixed-linker HKUST-1 have been tested for the catalytic oxidative coupling of benzylamine and 2-aminoacetophenone to form quinazoline, using TBHP as the oxidant. A progressive increase in the reaction rate is observed, paralleling the amount of OH-IP substitution, which we attribute to the presence of a mesopore system that mitigates diffusion limitations for the desorption of the bulky quinazoline product formed inside the MOF pores.

Author contributions

A.N.: investigation and writing – original draft. F.X.L.X.: conceptualization, funding acquisition, and writing – review & editing.

Conflicts of interest

There are no conflicts to declare.

Data availability

The data supporting this article have been included as part of the supplementary information (SI). Supplementary information: Table S1 (scope of the reaction), Fig. S1–S6 (^{1}H NMR spectra of acid digested **HM-1** and **HM-2**; TGA curves; representative FESEM images of all samples; hot-filtration test; XRD pattern of fresh and used **HM-2**; and FTIR spectra of adsorbed CO onto **M-1** and **HM-2**). See DOI: https://doi.org/10.1039/d6ma00417b.

All data will also be made available at the institutional repositories of the authors: Riunet (https://riunet.upv.es/home) and digital CSIC (https://digital.csic.es/).

Acknowledgements

Financial support from the Spanish Ministry of Science and Innovation (PID2023-146114NB-C21 and CEX2021-001230-S grants funded by MCIN/AEI/10.13039/501100011033) is gratefully acknowledged. This study forms part of the Advanced Materials Program and was supported by MICIN with funding from European Union NextGeneration (PRTR-C17.I1) and by the Generalitat Valenciana (MFA/2022/003).

References

1 A. Corma, H. Garcia and F. X. Llabrés i Xamena, *Chem. Rev.*, 2010, **110**, 4606–4655.
2 J. Gascon, A. Corma, F. Kapteijn and F. X. Llabrés i Xamena, *ACS Catal.*, 2014, **4**, 361–378.
3 S. M. J. Rogge, A. Bavykina, J. Hajek, H. Garcia, A. I. Olivos-Suarez, A. Sepúlveda-Escribano, A. Vimont, G. Clet, P. Bazin, F. Kapteijn, M. Daturi, E. V. Ramos Fernandez, F. X. Llabrés i Xamena, V. Van Speybroeck and J. Gascon, *Chem. Soc. Rev.*, 2017, **46**, 3134–3184.
4 H.-H. Mautschke, F. Drache, I. Senkovska, S. Kaskel and F. X. Llabrés i Xamena, *Catal. Sci. Technol.*, 2018, **8**, 3610–3616.
5 B. R. Saifutdinov, V. I. Isaeva, V. V. Chernyshev, V. V. Vergun, G. I. Kapustin, Y. P. Ivanova, M. M. Ilyin, O. P. Tkachenko, A. K. Buryak and L. M. Kustov, *Polymers*, 2022, **14**, 1373.
6 Y. Q. Lan, H. L. Jiang, S. L. Li and Q. Xu, *Adv. Mater.*, 2011, **23**, 5015–5020.
7 H. L. Jiang, Y. Tatsu, Z. H. Lu and Q. Xu, *J. Am. Chem. Soc.*, 2010, **132**, 5586–5587.
8 H. Y. Guan, R. J. LeBlanc, S. Y. Xie and Y. Yue, *Coord. Chem. Rev.*, 2018, **369**, 76–90.
9 J. Park, Z. U. Wang, L. B. Sun, Y. P. Chen and H. C. Zhou, *J. Am. Chem. Soc.*, 2012, **134**, 20110–20116.
10 Z. Fan, J. Wang, W. Wang, S. Burger, Z. Wang, Y. Wang, C. Wöll, M. Cokoja and R. A. Fischer, *ACS Appl. Mater. Interfaces*, 2020, **12**, 37993–38002.
11 W. R. Heinz, R. Junk, I. Agirrezabal-Telleria, B. Bueken, H. Bunzen, T. Gölz, M. Cokoja, D. De Vos and R. A. Fischer, *Catal. Sci. Technol.*, 2020, **10**, 8077–8085.
12 O. Kozachuk, I. Luz, F. X. Llabrés i Xamena, H. Noei, M. Kauer, H. B. Albada, E. D. Bloch, B. Marler, Y. Wang, M. Muhler and R. A. Fischer, *Angew. Chem., Int. Ed.*, 2014, 53, 7058–7062.
13 W. Zhang, M. Kauer, O. Halbherr, K. Epp, P. Guo, M. I. Gonzalez, D. J. Xiao, C. Wiktor, F. X. Llabrés i Xamena, C. Wöll, Y. Wang, M. Muhler and R. A. Fischer, *Chem. – Eur. J.*, 2016, **22**, 14297–14307.
14 S. He, Y. Chen, Z. Zhang, B. Ni, W. He and X. Wang, *Chem. Sci.*, 2016, **7**, 7101–7105.
15 K. M. Choi, H. J. Jeon, J. K. Kang and O. M. Yaghi, *J. Am. Chem. Soc.*, 2011, **133**, 11920–11923.
16 Z. Xin, J. Bai, Y. Pan, M. J. Zaworotko, Z. Xin, J. Bai, Y. Pan and M. J. Zaworotko, *Chem. – Eur. J.*, 2010, **16**, 13049–13052.
17 Z. Fang, J. P. Dürholt, M. Kauer, W. Zhang, C. Lochenie, B. Jee, B. Albada, N. Metzler-Nolte, A. Pöppl, B. Weber, M. Muhler, Y. Wang, R. Schmid and R. A. Fischer, *J. Am. Chem. Soc.*, 2014, **136**, 9627–9636.
18 B. Liu, Y. Li, S. C. Oh, Y. Fang and H. Xi, *RSC Adv.*, 2016, **6**, 61006–61012.
19 H. H. Mautschke and F. X. Llabrés i Xamena, *Chem. – Eur. J.*, 2021, **27**, 10766–10775.
20 G. A. Khodarahmi, E. Jafari, M. R. Khajouei, F. Hassanzadeh, G. H. Hakimelahi and G. A. Khodarahmi, *Res. Pharm. Sci.*, 2016, **11**, 1–14.
21 P. Kushwaha, A. Bhardwaj and Rashi, *Tetrahedron*, 2025, **179**, 134635.
22 C. Wang, S. Li, H. Liu, Y. Jiang and H. Fu, *J. Org. Chem.*, 2010, **75**, 7936–7938.
23 B. Han, X. L. Yang, C. Wang, Y. W. Bai, T. C. Pan, X. Chen and W. Yu, *J. Org. Chem.*, 2012, **77**, 1136–1142.
24 N. Anand, K. H. P. Reddy, T. Satyanarayana, K. S. R. Rao and D. R. Burri, *Catal. Sci. Technol.*, 2012, **2**, 570–574.
25 H. Yuan, W. J. Yoo, H. Miyamura and S. Kobayashi, *Adv. Synth. Catal.*, 2012, **354**, 2899–2904.
26 T. Truong, T. M. Hoang, C. K. Nguyen, Q. T. N. Huynh and N. T. S. Phan, *RSC Adv.*, 2015, **5**, 24769–24776.
27 J. Rouquerol, P. Llewellyn and F. Rouquerol, *Stud. Surf. Sci. Catal.*, 2007, **160**, 49–56.
28 D. A. Gómez-Gualdrón, P. Z. Moghadam, J. T. Hupp, O. K. Farha and R. Q. Snurr, *J. Am. Chem. Soc.*, 2016, **138**, 215–224.
29 E. P. Barrett, L. G. Joyner and P. P. Halenda, *J. Am. Chem. Soc.*, 1951, **73**, 373–380.
30 L. Valenzano, B. Civalleri, S. Chavan, S. Bordiga, M. H. Nilsen, S. Jakobsen, K. P. Lillerud and C. Lamberti, *Chem. Mater.*, 2011, **23**, 1700–1718.
31 K. S. W. Sing, D. H. Everett, R. A. W. Haul, L. Moscou, R. A. Pierotti, J. Rouquerol and T. Siemieniewska, *Pure Appl. Chem.*, 1985, **57**, 603–619.
32 S. S. Y. Chui, S. M. F. Lo, J. P. H. Charmant, A. G. Orpen and I. D. Williams, *Science*, 1999, **283**, 1148–1150.
33 M. Thommes, K. Kaneko, A. V. Neimark, J. P. Olivier, F. Rodriguez-Reinoso, J. Rouquerol and K. S. W. Sing, *Pure Appl. Chem.*, 2015, **87**, 1051–1069.
34 X. Yang, L. Qiao and W. Dai, *Chin. J. Catal.*, 2015, **36**, 1875–1885.
35 M. Shoaee, M. W. Anderson and M. P. Attfield, *Angew. Chem., Int. Ed.*, 2008, **47**, 8525–8528.
36 T. Liu, Y. Liu, L. Yao, W. Yang, L. Tian, H. Liu, D. Liu and C. Wang, *Nanoscale*, 2018, **10**, 13194–13201.
37 M. Shöâeè, J. R. Agger, M. W. Anderson and M. P. Attfield, *CrystEngComm*, 2008, **10**, 646–648.
38 R. Ameloot, F. Vermoortele, J. Hofkens, F. C. De Schryver, D. E. De Vos and M. B. J. Roeffaers, *Angew. Chem., Int. Ed.*, 2013, **52**, 401–405.
39 H. H. Mautschke and F. X. Llabrés i Xamena, *Molecules*, 2022, **27**, 6315.
40 S. Marx, W. Kleist and A. Baiker, *J. Catal.*, 2011, **281**, 76–87.